

A low-dimensional model for adaptive networks of spiking neurons

Bastian Pietras,¹ Pau Clusella,² and Ernest Montbrió¹

¹*Neuronal Dynamics Group, Department of Engineering, Universitat Pompeu Fabra, 08018 Barcelona, Spain.*

²*EPSEM, Departament de Matemàtiques, Universitat Politècnica de Catalunya, Manresa, Spain.*

(Dated: October 7, 2024)

We analyze a large ensemble of Quadratic Integrate-and-Fire (QIF) neurons with heterogeneous input currents and adaptation variables. For a particular class of adaptation, which we call quadratic spike-frequency adaptation (QSFA), the high-dimensional system admits an exact reduction to a low-dimensional system of ordinary differential equations for three mean-field variables: the population's firing rate, the mean membrane potential, and a mean adaptation variable. These low-dimensional firing rate equations (FRE) reveal an important generic feature of heterogeneous networks with spike frequency adaptation: Both the center and the width of the distribution of the neurons' firing frequencies are reduced, and this largely favors the emergence of collective synchronization in the network. These results are confirmed by the bifurcation analysis of the FRE, which faithfully describe the collective dynamics of the spiking neuron network, including collective oscillations, bursting, and macroscopic chaos.

PACS numbers:

I. INTRODUCTION

Neuronal firing rate equations (FREs) are mathematical descriptions of the collective activity of large ensembles of neurons, typically in form of one or a few ordinary differential equations [1–4]. These population models offer an approximate, coarse-grained description of the dynamics of spiking neuron networks—generally applicable near asynchronous states—and serve as valuable tools for both theoretical and computational analyses of large-scale neuronal dynamics.

Over the last decade, a singular class of firing rate equations has been obtained [5, 6]. These models, often referred to as ‘Next-Generation Neural Mass Models’ [7], are derived exactly from large networks of heterogeneous Quadratic Integrate-and-Fire (QIF) neurons, and offer two key advantages over traditional firing rate models: First, they provide an exact link between the microscopic dynamics of individual spiking neurons and the evolution of two macroscopic variables—mean firing rate and mean membrane potential. Second, they fully capture both transient dynamics and synchronous states in spiking neuron networks. Furthermore, the mean-field theory used to derive these exact firing rate equations, which is closely related to the Ott-Antonsen theory for populations of phase oscillators [8], is versatile enough to accommodate additional biological realism [7, 9–25]. As a result, these models have become very useful to investigate neuronal dynamics [26–33], and are powerful modeling tools in neuroscience [34–45].

A significant theoretical challenge remains in extending the theory to derive exact FREs for populations of QIF neurons with additional dynamic variables [85]. Several recent studies have developed approximate FREs seeking to describe the collective dynamics of such ‘extended’ QIF neurons [46–56]. A particular example are ensembles of QIF neurons with spike-frequency adaptation (SFA) [46, 47], which is a prominent feature of neuronal dynamics by which many neuron types reduce their firing frequencies in response to sustained current injection, see e.g. [57–60]. While an exact mean-field reduction of heterogeneous QIF neurons with SFA re-

mains elusive, some studies have approximated the QIF neuron model with SFA by assuming that the neuron-specific adaptation variables can be represented by a global adaptation variable that evolves according to the population’s firing rate [46, 47]. This approximation allows for an exact reduction of the spiking neuron network to a system of FREs, incorporating the additional adaptation dynamics, and captures key collective phenomena that are reminiscent of spiking networks with SFA, such as the emergence of collective synchronization (due to the presence of a slow negative feedback), and bursting.

However, important features of the microscopic dynamics related to the neuron-specific nature of SFA, which have significant implications at the population level, are not well described by such firing rate models. One overlooked effect, to the best of our knowledge, occurs in populations of neurons with SFA and heterogeneous firing frequencies (as in the models analyzed in [46, 47]): neurons with intrinsically high firing rates experience a greater reduction in firing frequency due to SFA than those with lower firing rates. Consequently, the overall level of frequency heterogeneity decreases, greatly favoring the emergence of collective synchronization [61, 62].

In this work, we take an alternative approach to reduce the dynamics of an extended QIF model with a specific form of SFA, termed Quadratic Spike-Frequency Adaptation (QSFA) [57], to an effectively one-dimensional QIF model [86]. This allows for analytical progress and the exact derivation of a low-dimensional system of FREs for large networks of heterogeneous QIF neurons with QSFA. In our approach, the adaptation variables remain neuron-specific, ensuring that neurons with higher intrinsic firing rates undergo greater adaptation than those with lower firing rates. This is reflected in an adaptation-induced reduction in the level of heterogeneity in the FREs, significantly enhancing the emergence of collective synchronization in the network.

The paper is structured as follows: In Section II, we introduce the generalized QIF model with SFA and describe the approximations leading to the QSFA model. We also illustrate the effects of QSFA on the steady states of QIF neuron pop-

ulations with heterogeneous inputs, demonstrating that QSFA results in both a shift and a narrowing of the firing rate distribution. In Section III, we outline the derivation of the FREs for a heterogeneous population of QIF neurons with QSFA. In Section IV, we analyze the bifurcations in the QIF-FRE model with QSFA and present phase diagrams that summarize the model's possible dynamic regimes. Additionally, we compare numerical simulations of the microscopic QIF network with those of the low-dimensional QIF-FRE model. Finally, in Section V, we summarize and discuss our findings.

II. POPULATIONS OF HETEROGENEOUS QIF NEURONS WITH SPIKE-FREQUENCY ADAPTATION (SFA)

We consider a population of N neurons with membrane potentials $V_{j=1,\dots,N}$, and membrane time constant τ_m , which evolve according to the following Quadratic Integrate-and-Fire (QIF) model [63–65]

$$\tau_m \dot{V}_j = V_j^2 + I_j - a_j, \quad (1a)$$

$$\tau_a \dot{a}_j = -a_j + \beta f_j. \quad (1b)$$

The last two terms on the r.h.s. of Eq. (1a) vary from neuron to neuron and represent, respectively, constant inputs and adaptation currents (of strength $\beta \geq 0$). The definition of the QIF model requires a resetting rule such that after each spike—which is marked by the spike time t_j^k at which V_j reaches infinity—the voltage is instantaneously reset to minus infinity. For the spike resetting at infinity, the spike-frequency (or firing rate) of intrinsically active neurons ($I_j - a_j > 0$) is [63, 64]

$$\nu_j = \frac{1}{\pi \tau_m} \sqrt{I_j - a_j},$$

and $\nu_j = 0$ for quiescent, or excitable, neurons ($I_j - a_j \leq 0$). The adaptation variables a_j obey the linear, first order differential equations Eq. (1b), where f_j measures the frequency of the spikes of neuron j . Spike-frequency adaptation (SFA) is often modeled by substituting the term f_j in Eq. (1b) with the spike train of neuron j , so that the adaptation variable a_j increases by a finite amount β/τ_a whenever neuron j undergoes an action potential [57–60, 65–73]; if neuron j does not spike, a_j decays with time constant $\tau_a \gg \tau_m$.

An important dynamical consequence of spike-dependent adaptation models is that they only slow down the firing frequency of intrinsically firing neurons ($I_j - a_j > 0$), but cannot stop their repetitive firing [58]; certainly, spike-dependent adaptation cannot initiate firing in those neurons that are intrinsically quiescent ($I_j - a_j \leq 0$), either. Hence, while the number of firing neurons remains the same, this dynamical feature changes the distribution of the neurons' firing frequencies by reducing not only its mean, but also its width.

A. Quadratic spike-frequency adaptation (QSFA) model

To simplify the analysis of the QIF model Eqs. (1), one may replace the discontinuous spike train of the spike-dependent

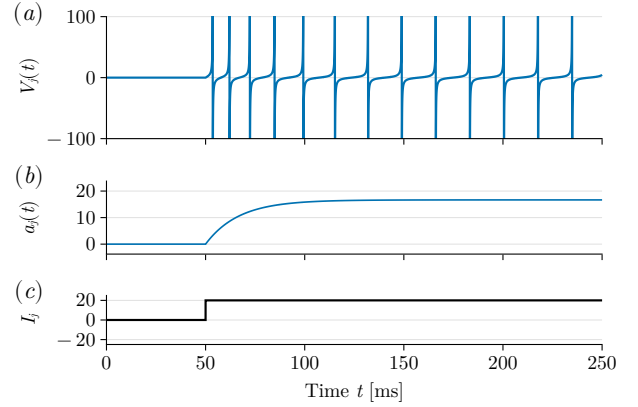


FIG. 1: Dynamics of a QIF neuron with QSFA, Eqs. (1 & 2). A spike train of an adapting neuron, in panel (a), is evoked by the onset of the stimulus shown in panel (c). Panel (b): For $t \geq 50$, the adaptation variable evolves as: $a_j(t) = I_j \beta / (1 + \beta) (1 - e^{-(t-50)(1+\beta)/\tau_a})$, and converges to $a_j^* = 50/3$, see Eq. (3). As adaptation builds up, the frequency of the spikes drops from an initially high onset rate to a lower, steady-state frequency given by Eq. (4). Parameters: $\beta = 5$ and $\tau_a = 10\tau_m = 100\text{ms}$.

adaptation model by a continuous, linear function of the instantaneous spike-frequency ν_j , i.e. $f_j \propto \nu_j$, see, e.g. [74]. Alternatively, here we propose the following quadratic spike-frequency adaptation (QSFA) model,

$$f_j = I_j - a_j, \quad (2)$$

in which f_j is proportional to the square of the spike-frequency of those neurons that are intrinsically active, i.e. $f_j \propto \nu_j^2$. Fig. 1(a) shows the time series of the voltage variable V_j of a quiescent QIF neuron with QSFA that receives a step input current at $t = 50\text{ms}$ and becomes self-oscillatory. Initially, the adaptation variable is $a_j(0) = 0$, and then exponentially converges to the fixed point of Eq. (1b),

$$a_j^* = \frac{\beta}{1+\beta} I_j. \quad (3)$$

Accordingly, the steady-state frequency the QIF neuron (often referred to as the neuron's f-I curve) is [87]

$$\nu_j = \frac{1}{\pi \tau_m} \sqrt{\frac{I_j}{1+\beta}}, \quad (4)$$

if $I_j > 0$, and $\nu_j = 0$ otherwise. Eq. (4) shows that it is exclusively the sign of I_j that determines the dynamical character of each neuron: QSFA either slows down the firing rate of intrinsically active neurons ($I_j > 0$) without stopping firing, or it brings quiescent neurons ($I_j < 0$) closer to their firing threshold, yet without inducing firing. The ratio between active and quiescent neurons thus remains the same. And while the frequencies f_j in Eq. (2) become negative for $I_j < 0$, this only alters the shape of the inputs' *subthreshold* distribution, but does not influence the level of activity of the population.

The choice of the QSFA model (2) has two benefits that critically simplify the study of the mean-field population model: First, Eqs. (1b) become independent of the particular state of

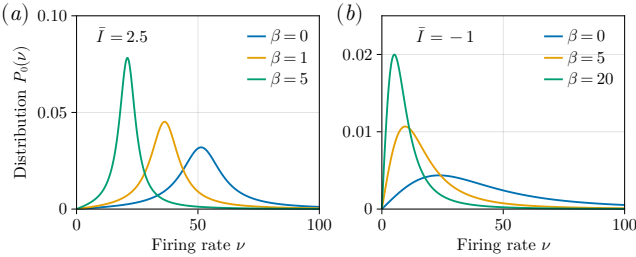


FIG. 2: Quadratic Spike-Frequency Adaptation (QSFA) reduces both the center and the width of the firing frequency distributions in populations of heterogeneous QIF neurons. We show the graph of Eq. (5) with a Lorentzian distribution of currents $g(I)$, for different levels of the adaptation strength β , and for a population where the majority of neurons are: (a) intrinsically spiking neurons, $\bar{I} = 2.5$; (b) quiescent neurons, $\bar{I} = -1$. In each case, the area under the three graphs is the same, indicating that QSFA does not alter the proportion of intrinsically spiking neurons in the population. Parameters: $\Delta = 1$, $\tau_m = 10\text{ms}$.

neuron j , so that the dynamics of the QIF neurons Eqs. (1a) becomes effectively one-dimensional. Second, due to the quadratic dependence of f_j on the neuron's frequency, the adaptation variables acquire the same distribution type as that of the parameters I_j . In particular, we will show that if both I_j and $a_j(0)$ are distributed according to a Lorentzian distribution, the variables a_j remain Lorentzian distributed at all times. Notably, this allows us to apply the technique originally proposed in [5] to derive an exact, low-dimensional system of FREs which exactly describes the dynamics of a population of QIF neurons with QSFA Eqs. (1&2) in the $N \rightarrow \infty$ limit.

B. Effect of QSFA on the distribution of firing frequencies

Before starting the derivation and analysis of the FRE with QSFA, it is illustrative to investigate the effect of QSFA on the steady-state distribution of firing frequencies of a population of (non-interacting) QIF neurons. We begin by identifying two important outcomes of Eq. (4) that generally occur in populations of extended QIF neurons Eqs. (1): Both the center and the width of the firing frequency distribution asymptotically shift to zero as the level of SFA is increased. That is, an overall decrease of activity in the population is accompanied by a global homogenization of the firing rates, compensating for the population's intrinsic heterogeneity. For the special case of QSFA, Eq. (3) shows the important property that the fixed point values a_j^* acquire the same distribution type as that of parameters I_j , where both the center and the width of the a_j^* distribution are scaled by the factor $\beta/(1+\beta)$. Effectively, this leads to a rescaling of both the center and the width of the I_j distribution by $1/(1+\beta)$. In consequence, the proportion of firing (or quiescent) neurons in the population is determined solely by the distribution of inputs I_j .

Finally, we explicitly compute the firing frequency distribution for QIF neurons with QSFA. Given a distribution $g(I)$ of inputs I_j , the (stationary) distribution of firing rates

$P_0(\nu) = g(I)|dI/d\nu|$, with $I(\nu) = (1+\beta)(\pi\tau_m\nu)^2$, satisfies

$$P_0(\nu) = 2(1+\beta)(\pi\tau_m)^2\nu g((1+\beta)(\pi\tau_m\nu)^2). \quad (5)$$

In Fig. 2, we show how this distribution changes with increasing adaptation strength $\beta > 0$ for a Lorentzian distribution of inputs I_j , $g(I) = \Delta/\pi[(I - \bar{I})^2 + \Delta^2]^{-1}$, of width Δ , and centered at positive ($\bar{I} = 2.5$) and negative ($\bar{I} = -1$) values. Increasing β shifts the center of the distribution to the left, and reduces its width. Integration of $P_0(\nu)$ shows that the area under the graphs is independent of β . This indicates that QSFA does not alter the proportion of intrinsically spiking neurons in the population, which is solely determined by $g(I)$.

III. FIRING RATE EQUATIONS WITH QUADRATIC SPIKE FREQUENCY ADAPTATION

In Section II, we have shown that QSFA strongly shapes the distribution of spike frequencies in populations of QIF neurons with distributed inputs. In the following, we demonstrate that this greatly influences the synchronization properties of large networks of recurrently coupled spiking neurons.

To investigate non-trivial collective dynamics of the QIF network Eqs. (1&2), we first extend our model so that neurons are able to interact with each other via a mean-field coupling. Specifically, hereafter we investigate the model Eqs. (1) with

$$I_j(t) = J\tau_m R(t) + \eta_j. \quad (6)$$

The first term consists of a mean-field excitatory coupling of strength $J > 0$. This coupling term is mediated by the population firing rate $R(t)$, which is obtained from the spike count function

$$S(t) = \frac{1}{N} \sum_{j=1}^N \sum_k \frac{1}{\tau} \int_{t-\tau}^t \delta(s - t_j^k) ds,$$

as $\lim_{\tau \rightarrow 0} S(t) = R(t)$. The terms η_j represent constant inputs that vary from neuron to neuron according to a Lorentzian distribution centered at $\bar{\eta}$ with half-width at half-maximum $\Delta > 0$:

$$g(\eta) = \frac{\Delta/\pi}{(\eta - \bar{\eta})^2 + \Delta^2}. \quad (7)$$

We now derive a low-dimensional system of differential equations (the so-called FREs) governing the evolution of the population firing rate R and mean voltage V of the population of QIF neurons. To this end, we first decompose the general solution of the linear ordinary differential equation Eq. (1b) with QSFA (2)

$$\tau_a \dot{a}_j = -(1+\beta)a_j + \beta [J\tau_m R(t) + \eta_j], \quad (8)$$

into two parts, as

$$a_j(t) = c_j e^{-t/\tau} + \alpha_j(t). \quad (9)$$

Since the first part of the solution decays exponentially to zero, the specific choice of the constants of integration c_j is irrelevant after a transitory period of the order of the lifetime

$$\tau = \frac{\tau_a}{1 + \beta}. \quad (10)$$

Still, for reasons that will become clear shortly, hereafter we consider that c_j are distributed according to a Lorentzian distribution centered at \bar{c} with half-width at half-maximum $\gamma > 0$

$$f(c) = \frac{\gamma/\pi}{(c - \bar{c})^2 + \gamma^2}. \quad (11)$$

The second component of the solution Eq. (9), $\alpha_j(t)$, is the particular solution of Eq. (8) with $a_j(0) = 0$. It is important to note that for Lorentzian distributed inputs η_j , the adaptation variables $\alpha_j(t)$ are also Lorentzian distributed [88].

Substituting Eqs. (6,9) into Eq. (1a) yields the QIF model

$$\tau_m \dot{V}_j = V_j^2 + J\tau_m R(t) + \eta_j - c_j e^{-t/\tau} - \alpha_j(t), \quad (12)$$

where η_j , c_j , and $\alpha_j(t)$ are all distributed according to Lorentzian probability density functions. Therefore, the model Eqs. (12) belongs to the class of models originally described in [5], that are amenable to an exact, low-dimensional description in terms of two mean-field quantities, the population mean firing rate and membrane potential.

Next, we follow [5] to derive a system of FRE that, in the thermodynamic limit $N \rightarrow \infty$, exactly describes the collective dynamics of the model Eqs. (12). Accordingly, we adopt the thermodynamic limit of Eqs. (1) and drop the indices in Eqs. (12,8). We denote by $\rho(V|\eta, c, t)$ the density of neurons with voltage V , given parameters η and c , whose evolution is governed by the continuity equation

$$\tau_m \partial_t \rho + \partial_V \left[\rho \left(V^2 + J\tau_m R + \eta - c e^{-t/\tau} - \alpha \right) \right] = 0. \quad (13)$$

Substituting the ‘Lorentzian ansatz’

$$\rho(V|\eta, c, t) = \frac{1}{\pi} \frac{X(\eta, c, t)}{[V - Y(\eta, c, t)]^2 + X(\eta, c, t)^2} \quad (14)$$

into Eq. (13), we find that, for each value of η and c , the variables X and Y satisfy

$$\tau_m \partial_t W = i \left[J\tau_m R + \eta - c e^{-t/\tau} - \alpha - W^2 \right], \quad (15)$$

where $W(\eta, c, t) \equiv X(\eta, c, t) + iY(\eta, c, t)$. The population firing rate is related with the variable $X(\eta, c, t)$ as

$$R(t) = \frac{1}{\pi\tau_m} \int_{-\infty}^{\infty} f(c) \int_{-\infty}^{\infty} X(\eta, c, t) g(\eta) d\eta dc, \quad (16)$$

and, since $Y(\eta, c, t)$ is the center of the distribution of membrane potentials $\rho(V|\eta, c, t)$, the (Cauchy principal value of the) integral of Y is the mean membrane potential

$$V(t) = \int_{-\infty}^{\infty} f(c) \int_{-\infty}^{\infty} Y(\eta, c, t) g(\eta) d\eta dc. \quad (17)$$

Eqs. (16) and (17) couple all the Eqs. (15) with each other. By considering the analytic continuation of W in the complex η and c planes, we require $\text{Re}(W)$ to not become negative. We thus consider the poles of $g(\eta)$ and $f(c)$ such that $\partial_t \text{Re}(W)|_{X=0} > 0$, i.e. $\eta = \bar{\eta} - i\Delta$ and $c = \bar{c} + i\gamma$ [89]. Then, by applying Cauchy’s residue theorem, we find that

$$W(\bar{\eta} - i\Delta, \bar{c} + i\gamma, t) = \pi\tau_m R(t) + iV(t). \quad (18)$$

The dynamics of R and V can be obtained from Eq. (15) after expanding the adaptation variable $\alpha(\eta, t)$ to the complex η -plane and evaluating it at the pole of $g(\eta)$, $\eta = \bar{\eta} - i\Delta$. Defining A and B as the real and imaginary parts of $\alpha(t, \bar{\eta} - i\Delta)$,

$$\alpha(t, \eta) = \alpha(t, \bar{\eta} - i\Delta) \equiv A(t) + iB(t), \quad (19)$$

and substituting Eqs. (18,19) into Eq. (15), yields the firing rate equations

$$\tau_m \dot{R} = \frac{1}{\pi\tau_m} \left[\Delta + \gamma e^{-t/\tau} + B \right] + 2RV, \quad (20a)$$

$$\tau_m \dot{V} = V^2 - (\tau_m \pi R)^2 + \bar{\eta} + J\tau_m R - A - \bar{c} e^{-t/\tau}, \quad (20b)$$

where the initial conditions $R(0) = r_0 \geq 0$ and $V(0) = v_0 \in \mathbb{R}$ correspond to the width and center, respectively, of the Lorentzian distribution of initial voltage variables $V_j(0)$. The evolution of the adaptation variable α can be determined by substituting Eq. (9) into Eq. (8) and then using Eq. (19). The solution of the imaginary part of the resulting equation is

$$B(t) = \frac{\Delta \beta (e^{-t/\tau} - 1)}{1 + \beta}, \quad (21)$$

whereas $A(t)$ obeys

$$\tau_a \dot{A} = -A(1 + \beta) + \beta [\bar{\eta} + J\tau_m R(t)], \quad (22)$$

with $A(0) = 0$. After a transitory period of the order of τ , the dynamics of Eq. (20) converges to the system of FRE

$$\tau_m \dot{R} = \frac{1}{\pi\tau_m} \frac{\Delta}{1 + \beta} + 2RV, \quad (23a)$$

$$\tau_m \dot{V} = V^2 - (\tau_m \pi R)^2 + \bar{\eta} + J\tau_m R - A. \quad (23b)$$

The three-dimensional system Eqs. (23,22) governs the asymptotic collective dynamics of the population of QIF neurons Eqs. (1,2,6), where $A(t)$ corresponds to the mean of the adaptation variables $a_j(t)$ [90].

IV. COLLECTIVE DYNAMICS OF POPULATIONS OF QIF NEURONS WITH QSFA

We next analyze the FREs (23,22) for globally coupled, excitatory QIF neurons with QSFA. We focus on the analysis of persistent states (PS), the onset of collective oscillations, as well as in the presence network bursts—that have been also found in spiking neuron networks with alternative models of SFA [46, 47, 65, 68, 73, 75]—and collective chaos.

It is well known that strong enough levels of recurrent excitation J may generally produce high activity, asynchronous

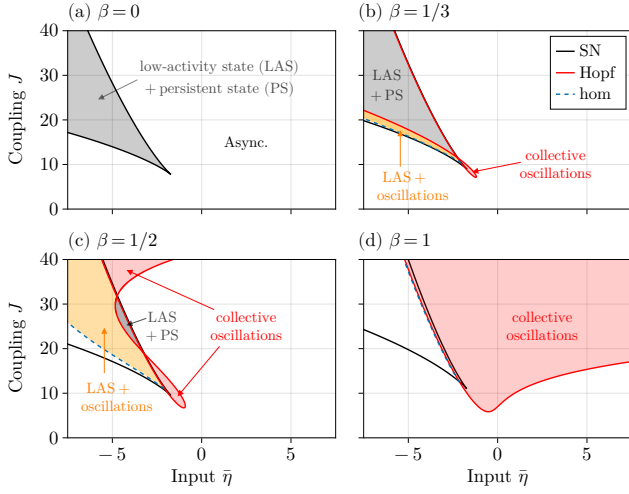


FIG. 3: Phase diagrams ($\bar{\eta}$, J) for increasing values of adaptation strength β . The Saddle-Node boundaries (SN, solid black lines) describe a cusp-shaped region of coexistence between low activity (LAS) and persistent (PS) states. Hopf and Homoclinic bifurcations correspond to the red and dashed blue boundaries, respectively. White regions: A fixed point corresponding to an asynchronous state is the only stable state. Gray-shaded regions: Bistability between two asynchronous states, LAS and PS. Red-shaded regions: Collective oscillations are the only stable state. Yellow-shaded regions: Bistability between LAS and collective oscillations. See also Fig. 4. Parameters: $\Delta = 1$, $\tau_a = 10\tau_m = 100\text{ms}$.

states in neural networks—so-called persistent states (PS). Although PS may be encountered in the presence of adaptation, we find that they are easily destabilized giving rise to oscillatory behavior. To investigate these instabilities, we first evaluate the fixed points of the FREs (23,22), which we write as [13]

$$R^* = \Phi(\bar{\eta} + J\tau_m R^*), \quad (24)$$

where the population's f-I curve is [91]

$$\Phi(I) = \frac{1}{\sqrt{1+\beta}} \frac{1}{\sqrt{2\pi\tau_m}} \sqrt{I + \sqrt{I^2 + \Delta^2}}. \quad (25)$$

QSFA does not alter the shape of the f-I curve, but only scales it by a factor $1/\sqrt{1+\beta}$, which allows us to borrow the parametric formula for the SN boundaries in [5] (corresponding to $\beta = 0$) and use it for any value of β [92]. The phase diagrams in Fig. 3 show two Saddle-Node (SN) bifurcation curves for various β values, which meet in a cusp point. Within the region bounded by the SN bifurcations, asynchronous, low-activity states (LAS) coexist with PS. In the rest of the parameter space there exists a unique fixed point that represents an asynchronous state.

In the absence of adaptation, LAS and PS are both stable in the gray-shaded region in Fig. 3(a). For increasing levels of adaptation, the PS is destabilized via a Hopf bifurcation, leading to collective oscillations in the yellow and red shaded regions of the diagram Fig. 3(b) [93]. For small β , the region where oscillations are the unique attractor (red-shaded in

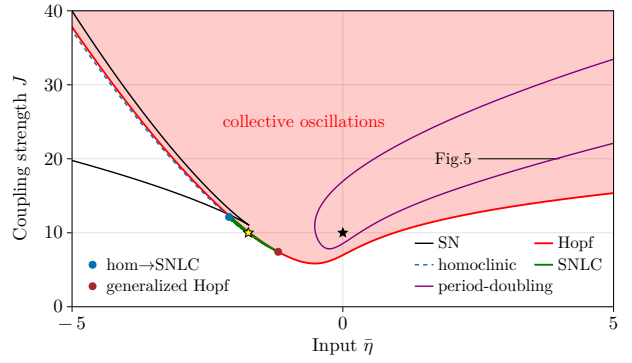


FIG. 4: Enlarged view of the phase diagram in Fig. 3d, corresponding to strong adaptation, $\beta = 1$. The diagram is dominated by the red-shaded region, where collective oscillations are the only stable attractor. For $\bar{\eta} < -1$, the Hopf bifurcation (Red lines) becomes subcritical at a generalized Hopf point (dark red dot), from where a saddle-node of limit cycle (SNLC) bifurcation emerges (green line). Close to the cusp-shaped SN bifurcation lines (black lines), the SNLC curve becomes a homoclinic bifurcation (blue dashed line) at the blue dot. Between the SNLC/homoclinic and the Hopf bifurcation curve, there is bistability between LAS and collective oscillations (the yellow star denotes the parameters of the numerical simulations shown in Fig. 6). Collective oscillations emerging from the Hopf curve can undergo secondary bifurcations: we found a period-doubling bifurcation (purple line, the black star denotes the parameters of the numerical simulations shown in Fig. 6) and within the period-doubling curve, there is a transition to chaotic collective dynamics through a period-doubling cascade (see Fig. 5).

Fig. 3) is restricted to a loop that pokes out of the cusp-shaped SN boundaries. As β is increased, the loop grows bigger and eventually unfolds almost parallel to the $\bar{\eta}$ -axis, leading to a vast region of oscillations in parameter space, see Fig. 3(c,d) and Fig. 4. Thus, sufficiently strong adaptation always leads to collective oscillations (provided that the strength of recurrent excitation J is large enough). This even occurs for $\bar{\eta} < 0$, that is, in networks in which the majority of the neurons are quiescent in absence of recurrent excitation.

The enhancement of collective oscillations by adaptation is greatly favored by the effects described in Section II, concerning the distribution of the neurons' firing frequencies, which are also clearly reflected in the FRE (23): The level of adaptation β effectively reduces heterogeneity Δ by a factor $1/(1+\beta)$, without altering the proportion of self-sustained oscillatory neurons in the population (by virtue of the reduction of the net input $\bar{\eta}$ by the same factor). This homogenization of the oscillators' natural frequencies promotes the emergence of collective synchronization [61, 62], which manifests at the collective level in the form of large-scale oscillations.

Finally, we investigate in more detail the bifurcations of the FREs (23,22) for $\beta = 1$, and demonstrate that the FREs perfectly predict and replicate the collective dynamics of the spiking network model Eqs. (1,2,6). Fig. 4 shows a detailed picture of the phase diagram in Fig. 3(d). First, we point out that the Hopf bifurcation is supercritical for positive values of $\bar{\eta}$, and becomes subcritical around $\bar{\eta} \approx -1$, in a generalized

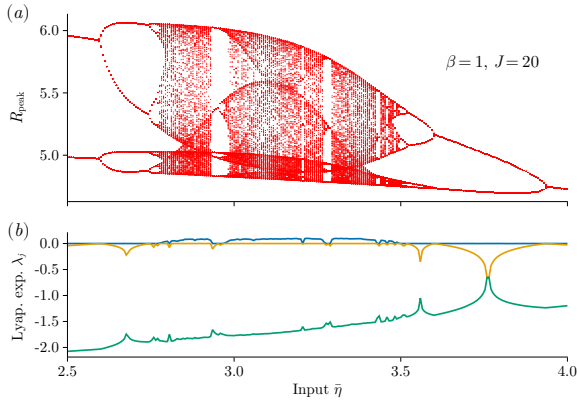


FIG. 5: Macroscopic chaotic behavior in the QIF model with QSFA emerges through a period-doubling cascade to chaos. (a) Peak values R_{peak} of the population’s firing rate $R(t)$ during complex oscillatory activity. (b) Lyapunov exponents computed with the FREs (23,22). A positive Lyapunov exponent indicates the presence of macroscopic chaos. Parameters as in Fig. 4.

Hopf bifurcation (dark-red dot). This gives rise to a small region of bistability between the asynchronous fixed point and a limit cycle (around the yellow star in Fig. 4), which is destroyed in a Saddle-Node bifurcation of limit cycles (SNLC). Additionally, immediately after the SNLC bifurcation crosses the lower SN bifurcation—entering the region of coexistence between LAS and PS—the stable limit cycle collides with the saddle point created in the SN bifurcation (blue dot), and oscillations are lost in a homoclinic bifurcation (blue dashed line). On the other hand, we find that collective oscillations also undergo period-doubling bifurcations, which are always present for positive $\bar{\eta}$. Inspecting the region within the period-doubling boundary more closely, reveals a period-doubling cascade leading to macroscopic chaos. Collective chaos can already be found for small values of QSFA-strength β and thus seems a generic dynamic feature of networks of QIF neurons with adaptation, see Appendix B.

In Fig. 6, we compare the dynamics of the FRE (23,22), with that of the original network model Eqs. (1,2,6), using numerical simulations. We show time series of the mean field variables R , V , and A for the two models, as well as a raster plot of the microscopic network. We initially set the parameters of the models in the bistable region of Fig. 4—indicated with a yellow star—and select initial conditions in such a way that the systems converge to the asynchronous fixed point. Then, at $t = 1.5$ s, the input $\bar{\eta}$ instantaneously increases from $\bar{\eta} = 0$ to $\bar{\eta} = 1.74$, and the systems are placed in a region near the period-doubling bifurcation—black star in Fig. 4. As the systems transition from the asynchronous regime to the new oscillatory state, they display identical transitory dynamics. Finally, at $t = 2.5$ s, the parameter $\bar{\eta}$ instantaneously returns to its initial value, but now the systems do not return to the fixed point, but they are attracted to the stable limit cycle. These simulation results confirm the validity of the low-dimensional FREs (23,22) to faithfully predict and reproduce the dynamics of the original, high-dimensional network model.

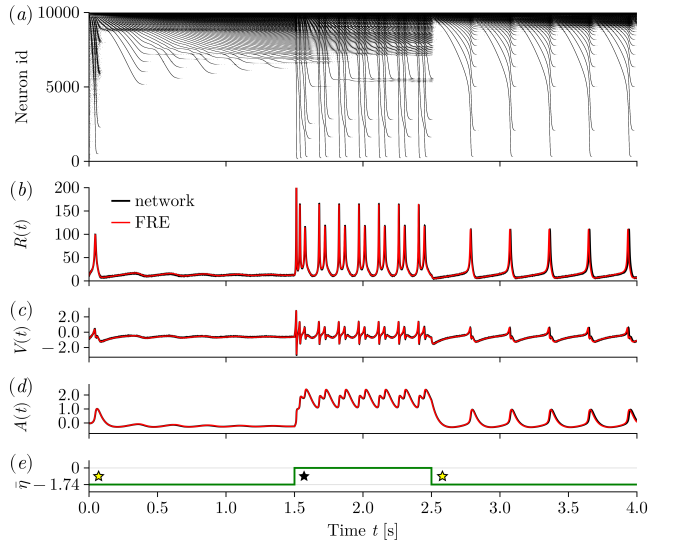


FIG. 6: QIF network simulations of $N = 10^4$ neurons with QSFA follow the exact FRE (23). An asynchronous low-activity state co-exists with network bursts (cf. dynamics for $t \leq 1.5$ s with those for $t > 2.5$ s), while an increase in external input drives the collective dynamics into complex collective oscillations ($1.5 < t \leq 2.5$ s). From top to bottom: Raster plot of the neurons ordered according to their inputs η_j , population firing rate $R(t)$, mean voltage $V(t)$, mean adaptation $A(t)$. Parameters: $\tau_m = 10$ ms, $\tau_a = 100$ ms, $J = 10$, $\Delta = 1$ and $\bar{\eta} = -1.74$, for $t \leq 1.5$ s and $t > 2.5$ s, and $\bar{\eta} = 0$ for $1.5 < t \leq 2.5$ s, see yellow and black stars in Fig. 4. For simulation details, see Appendix A.

V. CONCLUSIONS

Firing rate models have been exactly derived for populations of QIF neurons [5, 6], and extended to incorporate various forms of synaptic transmission [7, 10–17], connectivity structures [9, 76], neuronal heterogeneities [77–79], and noise [19–25]. However, the reduction method to obtain exact FREs is limited to ensembles of one-dimensional QIF neurons. This restriction poses a challenge for investigating networks that exhibit important dynamical features, such as spike-frequency adaptation (SFA).

In this work, we propose a QIF model that incorporates a quadratic SFA variable, whose evolution depends solely on the parameters of the QIF model and not on an individual neuron’s spike train. This feature effectively renders the model one-dimensional, but it retains the characteristic slowing down of the neuron’s firing frequency in response to an injected current. Due to the quadratic dependence of the adaptation variable on the neuron’s firing rate, the adaptation currents asymptotically match the distribution of the QIF model’s input currents. Consequently, the reduction method originally proposed in [5] can be applied. The resulting exact FREs capture the neuron-specific nature of SFA—neurons with higher firing rates undergo greater adaptation than those with lower firing rates—which is reflected in the FREs as a decrease in population heterogeneity and a global reduction in activity.

We demonstrate that this adaptation-induced homogeniza-

tion significantly enhances the emergence of global oscillations in the network (see Fig. 2) compared to models without neuron-specific SFA. In those models, the synchronization region is confined to a narrower parameter space (cf. Fig. 2 in [47]): The collective effect of SFA in models without neuron-specific adaptation variables reduces the intrinsic currents for each neuron by the same amount, turning intrinsically spiking neurons into quiescent neurons. This global reduction leads to the suppression of collective oscillations under strong adaptation conditions as the homogenization effect is lacking.

In the QIF model with QSFA, we observed macroscopic chaotic behavior characterized by a period-doubling route to chaos, which already appears at small levels of SFA (Fig. S2) and becomes more pronounced with stronger SFA (Fig. 5). Interestingly, neither collective chaos nor subcritical Hopf bifurcations have been reported in firing rate models for QIF neurons with global SFA [46, 47]. However, a similar generalized Hopf point—separating subcritical from supercritical Hopf bifurcations—was identified in [68], along with a large region of collective oscillations for strong recurrent excitation and adaptation, in agreement with our findings.

Our numerical simulations of the exact FRE (23,22) closely follow those of the original network model Eqs. (1,2,6), as expected, see Fig. 6. Still, we advise caution when interpreting results from microscopic network simulations due to the pres-

ence of finite-size fluctuations. In the QSFA model (1b,2), the adaptation variable is allowed to take on negative values. This ‘negative adaptation’ increases the excitability of quiescent neurons by reducing the distance between their resting potential and the spiking threshold, allowing finite-size fluctuations to induce population bursts that would not occur in infinitely large networks, or in SFA models where adaptation is constrained to non-negative values.

Several studies have explored the mechanisms by which SFA synchronizes neural firing [67, 68, 73, 80]. However, to our knowledge, the ability of SFA to reduce frequency heterogeneity within a neuronal population has been largely overlooked. Frequency heterogeneity plays a crucial role in determining the synchronization of a population of oscillators [61, 62]. Therefore, we believe that the synchronization effects that we reported, which are described by the firing rate model Eqs. (23,22), may provide new insights into the mechanistic origins of neuronal oscillations.

Acknowledgements. B.P. has received funding from the European Union’s Horizon 2020 research and innovation programme under the Marie Skłodowska-Curie grant agreement No 101032806. EM acknowledges support by the Agencia Estatal de Investigación under the Project No. PID2019-109918GB-I00, and by the Generalitat de Catalunya under the grant 2021SGR01522 646.

-
- [1] H. R. Wilson and J. D. Cowan, *Biophys. J.* **12**, 1 (1972).
 - [2] G. B. Ermentrout and D. H. Terman, *Mathematical foundations of neuroscience*, vol. 64 (Springer, 2010).
 - [3] G. Deco, V. K. Jirsa, P. A. Robinson, M. Breakspear, and K. Friston, *PLoS Computational Biology* **4**, e1000092 (2008).
 - [4] S. Coombes and K. C. Wedgwood, *Neurodynamics: An Applied Mathematics Perspective*, vol. 75 (Springer Nature, 2023).
 - [5] E. Montbrió, D. Pazó, and A. Roxin, *Phys. Rev. X* **5**, 021028 (2015).
 - [6] T. B. Luke, E. Barreto, and P. So, *Neural Comput.* **25**, 3207 (2013).
 - [7] S. Coombes and Á. Byrne, in *Nonlinear Dynamics in Computational Neuroscience*, edited by F. Corinto and A. Torcini (Springer International Publishing, Cham, 2019), pp. 1–16.
 - [8] E. Ott and T. M. Antonsen, *Chaos* **18**, 037113 (2008).
 - [9] C. R. Laing, *Phys. Rev. E* **90**, 010901 (2014).
 - [10] C. R. Laing, *SIAM Journal on Applied Dynamical Systems* **14**, 1899 (2015).
 - [11] I. Ratas and K. Pyragas, *Phys. Rev. E* **94**, 032215 (2016).
 - [12] D. Pazó and E. Montbrió, *Phys. Rev. Lett.* **116**, 238101 (2016).
 - [13] F. Devalle, A. Roxin, and E. Montbrió, *PLoS Computational Biology* **13**, 1 (2017).
 - [14] B. Pietras, F. Devalle, A. Roxin, A. Daffertshofer, and E. Montbrió, *Phys. Rev. E* **100**, 042412 (2019).
 - [15] E. Montbrió and D. Pazó, *Phys. Rev. Lett.* **125**, 248101 (2020).
 - [16] P. Clusella, E. Köksal-Ersöz, J. García-Ojalvo, and G. Ruffini, *Biological Cybernetics* **117**, 5 (2023).
 - [17] B. Pietras, *Neural Computation* **36**, 1476 (2024).
 - [18] V. Pyragas and K. Pyragas, *Phys. Rev. E* **105**, 044402 (2022).
 - [19] P. Clusella and E. Montbrió, *Phys. Rev. E* **109**, 014229 (2024).
 - [20] V. Pyragas and K. Pyragas, *Phys. Lett. A* p. 128972 (2023).
 - [21] B. Pietras, R. Cestnik, and A. Pikovsky, *Phys. Rev. E* **107**, 024315 (2023).
 - [22] D. S. Goldobin, E. V. Permyakova, and L. S. Klimenko, *Chaos: An Interdisciplinary Journal of Nonlinear Science* **34**, 013121 (2024).
 - [23] D. S. Goldobin, M. di Volo, and A. Torcini, *Phys. Rev. Lett.* **127**, 038301 (2021).
 - [24] D. S. Goldobin, *Chaos* **31** (2021).
 - [25] M. Di Volo, M. Segneri, D. S. Goldobin, A. Politi, and A. Torcini, *Chaos* **32** (2022).
 - [26] G. Dumont, G. B. Ermentrout, and B. Gutkin, *Phys. Rev. E* **96**, 042311 (2017).
 - [27] A. Byrne, D. Avitabile, and S. Coombes, *Phys. Rev. E* **99**, 012313 (2019).
 - [28] H. Schmidt and D. Avitabile, *Chaos* **30**, 033133 (2020).
 - [29] D. Avitabile, M. Desroches, and G. B. Ermentrout, *PLoS Comput. Biol.* **18**, e1010569 (2022).
 - [30] H. Taher, D. Avitabile, and M. Desroches, *Nonlinear Dynamics* **108**, 4261 (2022).
 - [31] V. V. Klinshov and S. Y. Kirillov, *Phys. Rev. E* **106**, L062302 (2022).
 - [32] C. R. Laing and O. E. Omel’chenko, *Biological Cybernetics* **117**, 259 (2023).
 - [33] R. Barrio, J. A. Jover-Galtier, A. Mayora-Cebollero, C. Mayora-Cebollero, and S. Serrano, *Phys. Rev. E* **109**, 014301 (2024).
 - [34] Á. Byrne, M. J. Brookes, and S. Coombes, *Journal of Computational Neuroscience* **43**, 143 (2017).
 - [35] H. Schmidt, D. Avitabile, E. Montbrió, and A. Roxin, *PLoS Computational Biology* **14**, 1 (2018).
 - [36] G. Dumont and B. Gutkin, *PLOS Computational Biology* **15**, 1 (2019).
 - [37] S. Keeley, Á. Byrne, A. Fenton, and J. Rinzel, *J. Neurophys.*

- 121**, 2181 (2019).
- [38] M. Segneri, H. Bi, S. Olmi, and A. Torcini, *Frontiers in Computational Neuroscience* **14**, 47 (2020).
- [39] M. Gerster, H. Taher, A. Škoch, J. Hlinka, M. Guye, F. Bartolomei, V. Jirsa, A. Zakharova, and S. Olmi, *Frontiers in Systems Neuroscience* **15**, 675272 (2021).
- [40] G. Rabuffo, J. Fousek, C. Bernard, and V. Jirsa, *eNeuro* **8** (2021).
- [41] D. Reyner-Parra and G. Huguet, *PLoS Comput. Biol.* **18**, e1009342 (2022).
- [42] Á. Byrne, J. Ross, R. Nicks, and S. Coombes, *Brain Topography* **35**, 36 (2022).
- [43] Y. S. Perl, G. Zamora-Lopez, E. Montbrió, M. Monge-Asensio, J. Vohryzek, S. Fittipaldi, C. G. Campo, S. Moguilner, A. Ibañez, E. Tagliazucchi, et al., *Network Neuroscience* **7**, 632 (2023), ISSN 2472-1751.
- [44] R. Gast, S. A. Solla, and A. Kennedy, *Proceedings of the National Academy of Sciences* **121**, e2311885121 (2024).
- [45] M. K. Nandi, M. Valla, and M. Di Volo, *Frontiers in Computational Neuroscience* **18**, 1422159 (2024).
- [46] R. Gast, H. Schmidt, and T. R. Knösche, *Neural Computation* **32**, 1615 (2020).
- [47] A. Ferrara, D. Angulo-Garcia, A. Torcini, and S. Olmi, *Phys. Rev. E* **107**, 024311 (2023).
- [48] L. Chen and S. A. Campbell, *J. Comput. Neurosci.* **50**, 445 (2022).
- [49] H. Taher, A. Torcini, and S. Olmi, *PLoS Comput. Biol.* **16**, e1008533 (2020).
- [50] R. Gast, T. R. Knösche, and H. Schmidt, *Phys. Rev. E* **104**, 044310 (2021).
- [51] I. Guerreiro, M. di Volo, and B. Gutkin, arXiv:2206.10370 (2022).
- [52] J. Xu, J. Wang, Q. Xu, J. Fang, and J. Qiu, *Nonlinear Dyn.* (2023).
- [53] C. G. Andersen, C. Duprat, A. Ezzati, P. Houzelstein, A. Ledoux, Y. Liu, S. Saghir, A. Destexhe, F. Tesler, and D. Depannemaeker, *Neural Computation* **36**, 1433 (2024).
- [54] L. Chen and S. A. Campbell, *SIAM Journal on Applied Dynamical Systems* **23**, 2293 (2024).
- [55] D. Depannemaeker, C. Duprat, M. Angioletti, C. S. Carbonell, H. Wang, S. Petkoski, P. Sorrentino, H. Sheheitli, and V. Jirsa, *bioRxiv* (2024).
- [56] H. Sheheitli and V. Jirsa, *Journal of Computational Neuroscience* **52**, 207 (2024).
- [57] J. Benda and A. V. M. Herz, *Neural Computation* **15**, 2523 (2003).
- [58] B. Gutkin and F. Zeldnerust, *Scholarpedia* **9**, 30643 (2014).
- [59] J. Benda and J. Tabak, *Spike-Frequency Adaptation* (Springer New York, New York, NY, 2022), pp. 3248–3258.
- [60] C. Börgers, *An introduction to modeling neuronal dynamics*, vol. 66 (Springer, 2017).
- [61] A. T. Winfree, *J. Theor. Biol.* **16**, 15 (1967).
- [62] Y. Kuramoto, *Chemical Oscillations, Waves, and Turbulence* (Springer-Verlag, Berlin, 1984).
- [63] B. Ermentrout and N. Kopell, *SIAM J. Appl. Math.* **46**, 233 (1986).
- [64] E. M. Izhikevich, *Dynamical Systems in Neuroscience* (The MIT Press, Cambridge, Massachusetts, 2007).
- [65] P. Latham, B. Richmond, P. Nelson, and S. Nirenberg, *Journal of Neurophysiology* **83**, 808 (2000).
- [66] X.-J. Wang, *Journal of Neurophysiology* **79**, 1549 (1998).
- [67] G. Fuhrmann, H. Markram, and M. Tsodyks, *Journal of Neurophysiology* **88**, 761 (2002).
- [68] G. Gigante, M. Mattia, and P. D. Giudice, *Phys. Rev. Lett.* **98**, 148101 (2007).
- [69] T. Schwalger and B. Lindner, *Frontiers in Computational Neuroscience* **7**, 164 (2013).
- [70] M. Augustin, J. Ladenbauer, F. Baumann, and K. Obermayer, *PLoS Comput. Biol.* **13**, e1005545 (2017).
- [71] T. Schwalger, M. Deger, and W. Gerstner, *PLoS Comput. Biol.* **13**, e1005507 (2017).
- [72] M. Di Volo, A. Romagnoni, C. Capone, and A. Destexhe, *Neural computation* **31**, 653 (2019).
- [73] C. v. Vreeswijk and D. Hansel, *Neural Computation* **13**, 959 (2001).
- [74] B. Ermentrout, *Neural Comput.* **10**, 1721 (1998).
- [75] M. Dur-e Ahmad, W. Nicola, S. A. Campbell, and F. K. Skinner, *J. Comput. Neurosci.* **33**, 21 (2012).
- [76] J. M. Esnaola-Acebes, A. Roxin, D. Avitabile, and E. Montbrió, *Phys. Rev. E* **96**, 052407 (2017).
- [77] V. Pyragas and K. Pyragas, *Phys. Lett. A* **416**, 127677 (2021).
- [78] M. di Volo and A. Torcini, *Phys. Rev. Lett.* **121**, 128301 (2018).
- [79] R. Gast, S. A. Solla, and A. Kennedy, *Physical Review E* **107**, 024306 (2023).
- [80] B. Ermentrout, M. Pascal, and B. Gutkin, *Neural Computation* **13**, 1285 (2001).
- [81] R. Cestnik and E. A. Martens, *Phys. Rev. Lett.* **132**, 057201 (2024).
- [82] D. Pazó, *Physics* **17**, 12 (2024).
- [83] E. Ott and T. M. Antonsen, *Chaos* **27**, 051101 (2017).
- [84] B. Ermentrout, *Neural Comp.* **8**, 979 (1996).
- [85] See [81, 82] for an interesting line of research in this direction.
- [86] A similar approach was used by Ott & Antonsen in Ref. [83], to investigate a variant of the Kuramoto model with a mechanism of frequency adaptation. We emphasize that in the model proposed by Ott & Antonsen the oscillator natural frequencies adapt to the frequency of the Kuramoto order parameter. By contrast, in SFA the degree of adaptation is independent of the level of synchrony, and depends only on the firing frequency of each neuron.
- [87] The effect of QSFA is the rescaling of the f-I curve by a factor $1/\sqrt{1+\beta} < 1$. The square root input dependence of Eq. (4) is characteristic of quadratic SFA models [57], whereas in linear SFA models (with $f_j \propto \nu_j$), the f-I curve scales linearly with the input near the onset of firing [66, 74].
- [88] The particular solution of the linear differential Eq. (8) with $a_j(0) = 0$ has the form
- $$\alpha_j(t) = \eta_j h(t) + l(t), \quad (26)$$
- with $l(t) = \beta J \tau_m / \tau_a \int_0^t e^{(t'-t)/\tau} R(t') dt'$, and $h(t) = (1 - e^{-t/\tau}) \beta / (1 + \beta)$. Thus, variables $\alpha_j(t)$ have the same distribution type as that of parameters η_j .
- [89] This can be seen by substituting Eq. (26) in Eq. (15) with $X(t) = R(t) = 0$, which yields
- $$\tau_m \partial_t W|_{X=0} = i \left[\eta - \eta h(t) - l(t) - ce^{-t/\tau} + Y^2 \right].$$
- Then, for $X = \text{Re}(W)$, the derivative $\partial_t X(t)$ evaluated at $X(t) = 0$ can be evaluated using complex-valued η and c , as
- $$\tau_m \partial_t X|_{X=0} = -\eta_i(1 - h) + c_i e^{-t/\tau} > 0,$$
- where the subscript i indicates the imaginary parts of η and c . Given that $h \in [0, 1]$, this can be independently satisfied (either for $\eta_i \neq 0 = c_i$, or for $c_i \neq 0 = \eta_i$) only if $\eta_i < 0$ or $c_i > 0$.
- [90] After a transitory period of time τ , the variables $A(t)$ and $|B(t)|$ correspond to the mean and the spread of the neurons'

adaptation variables $a_j(t)$. The solution Eq. (21) indicates that the width of the distribution of adaptation variables is reduced by the factor $\beta/(1+\beta)$. If $\bar{\eta}$ is time-independent, the solution of Eq. (22) can be written as $A(t) = \bar{\eta}(1 - e^{-t\tau})/(1 + \beta) + \tilde{A}(t)$ where $\tilde{A}(t)$ follows the dynamics $\tau_a \dot{\tilde{A}} = -\tilde{A}(1 + \beta) + \beta J \tau_m R(t)$. Therefore, after a transient of the order τ , the solution is $A(t) = \bar{\eta}/(1 + \beta) + \tilde{A}(t)$, and the center of the distribution of adaptation variables is also reduced by a factor $\beta/(1 + \beta)$.

- [91] Similar to the f-I curve of an individual QIF neuron with QSFA, Eq. (4), also the population f-I curve Φ is a non-negative, monotonously increasing function that scales as the square root of the input for large I .
- [92] In parametric form, the SN curves —shown in Fig. 3— are:

$$\bar{\eta}_{SN} = -(1 + \beta)(\pi \tau_m R^*)^2 - \frac{3\Delta^2}{4(1 + \beta)(\pi \tau_m R^*)^2},$$

and

$$J_{SN} = 2(1 + \beta)\pi^2 \tau_m R^* + \frac{\Delta^2}{2(1 + \beta)\pi^2 (\tau_m R^*)^3}.$$

- [93] See Appendix B 1 and Figs. S1,S2 for a more detailed picture of this bifurcation scenario.

Appendix A: Numerical simulation of QIF neurons with QSFA

Microscopic network simulations of QIF neurons with QSFA, Eqs. (1,2,6), were performed using the equivalent θ -neuron formulation via $V_j = \tan(\theta_j/2)$ [84]:

$$\begin{aligned} \tau_m \dot{\theta}_j &= 1 - \cos \theta_j + (1 + \cos \theta_j)[\eta_j - a_j + J \tau_m R(t)], \\ \tau_a \dot{a}_j &= -a_j + \beta[\eta_j - a_j + J \tau_m R(t)], \end{aligned}$$

with time step $dt = 10^{-3} \tau_m$, $\tau_m = 10\text{ms}$ and $\tau_a = 100\text{ms}$. The mean firing rate $R(t)$ was computed via the conformal mapping of the complex-valued Kuramoto order parameter $Z(t)$ [5, 21]:

$$R(t) = \frac{1}{\pi} \operatorname{Re} \left\{ \frac{1 - Z^*(t)}{1 + Z^*(t)} \right\}, \quad Z(t) = \frac{1}{N} \sum_{j=1}^N e^{i\theta_j(t)};$$

the asterisk denotes complex conjugation. The mean voltage was computed as $V(t) = \operatorname{Im}\{[1 - Z^*(t)]/[1 + Z^*(t)]\}$. The mean adaptation, $\bar{A}(t) = \sum_{j=1}^N a_j(t)/N$, converges to $A(t)$ in the limit $N \rightarrow \infty$. In Fig. 6, the voltage variables $V_j(0)$ of the $N = 10^4$ neurons are initially distributed according to a Lorentzian centered at $v_0 = -0.8$ with half-width at half-maximum $\pi r_0 = 10\pi$ and the adaptation variables $a_j(0) = 0$ follow a Dirac- δ distribution (which belongs to the class of Lorentzian distributions). This allows an immediate fit with the FREs (23,22) with $R(0) = r_0$, $V(0) = v_0$ and $A(0) = 0$.

Appendix B: Analysis of the QIF-FRE with QSFA

1. SFA destabilizes persistent states

The phase diagram for the collective dynamics of QIF neurons without QSFA (see Fig. 3(a) with $\beta = 0$) is dominated by Saddle-Node (SN) bifurcation curves that form a cusp-shaped bistability region, where two asynchronous states coexist: a low-activity state (LAS) and a high-activity, so-called persistent state (PS). The cusp-shaped region is similar with and without QSFA by virtue of the f-I curve Φ , cf. Eq. (25) and Fig. 3. However, already small values of QSFA induce oscillatory instabilities, where the stationary LAS and PS lose stability via Hopf bifurcations, see, e.g., Fig. S1 for $\beta = 1/3$. Here, the subcritical Hopf bifurcation on the lower branch occurs just before the SN point, gives rise to an unstable limit cycle solution, and therefore slightly cuts back on the bistability region. The supercritical Hopf bifurcation on the top branch gives rise to a stable limit cycle solution and, thus, also cuts back on the bistability region of coexisting LAS and PS (the gray-shaded region in Fig. S1a). Moreover, the limit-cycle solution soon undergoes a period-doubling bifurcation and ends in a homoclinic bifurcation (also before the SN bifurcation, see Fig. S1b). As the limit cycle has quite a constricted basin of attraction—we invite the interested reader to actually find the cycling solution for a given mean input $\bar{\eta}$ —, the bistability between the LAS and the oscillatory solution (yellow-shaded in Fig. S1a) de facto collapses to the LAS. In sum, QSFA destabilizes persistent states and destroys bistability.

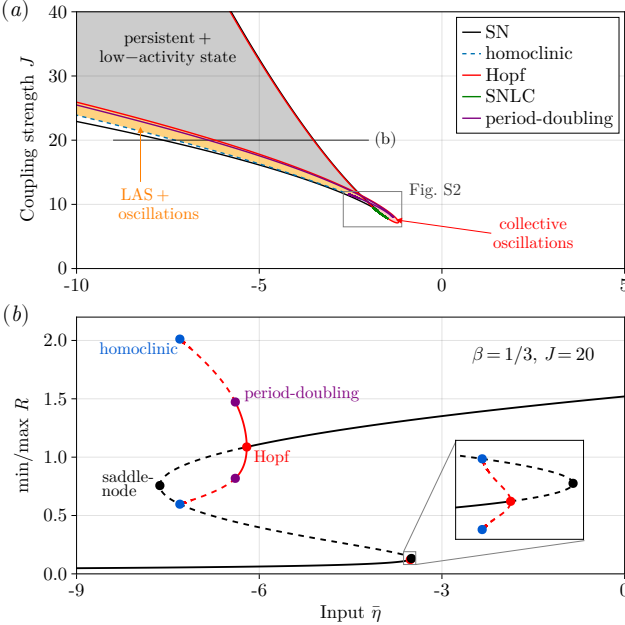


FIG. S1: SFA destroys bistability. (a) Phase diagram in $\bar{\eta} - J$ -plane for $\beta = 1/3$. (b) Bifurcation diagram R^* vs. $\bar{\eta}$ for $\beta = 1/3, J = 20$.

2. Collective oscillations, network bursts, and chaos

Collective oscillations become the dominant, and unique, attractor in the phase diagram with QSFA ($\beta > 0$). For small QSFA-strengths, $\beta = 1/3$, the bifurcation scenario is somewhat intricate: Collective oscillations are constrained to the loop that pokes out of the cusp-shaped (mostly unstable) SN boundaries (see Fig. S2 for a zoom into the loop in Fig. S1a). In the bifurcation diagram Fig. S2(b), we fix the recurrent excitation at $J = 9$ and decrease the mean input $\bar{\eta}$ from -1.4 to -1.8 . At $\bar{\eta} \approx -1.5$, the PS destabilizes through a supercritical Hopf bifurcation and gives rise to stable periodic oscillations. Subsequently, the oscillatory state undergoes a cascade of period-doubling bifurcations into macroscopic chaos around $\bar{\eta} \approx -1.53$ (Fig. S2c). Close to these parameter values, there are tiny regions where the single-periodic solution regains stability (solid green curves in the insets of Fig. S2b), which are bounded by Saddle-Node of Limit Cycle bifurcations (SNLC, green dot) and period-doubling bifurcations (magenta dot). For smaller $\bar{\eta} < -1.56$, the single-periodic solution restabilizes, though the time series of the firing rate $R(t)$ feature two peaks during each cycle (Fig. S2c). Around $\bar{\eta} \approx -1.78$, the periodic solution loses stability in a SNLC bifurcation and the unstable branch connects to the LAS in a subcritical Hopf bifurcation (red dot in Fig. S2b), creating a small region of bistability between a limit cycle and the LAS.

3. Stronger QSFA facilitates collective oscillations and chaos

As shown in Fig. 3, the region of collective oscillations increases for larger QSFA-strengths β . The tiny loop of domi-

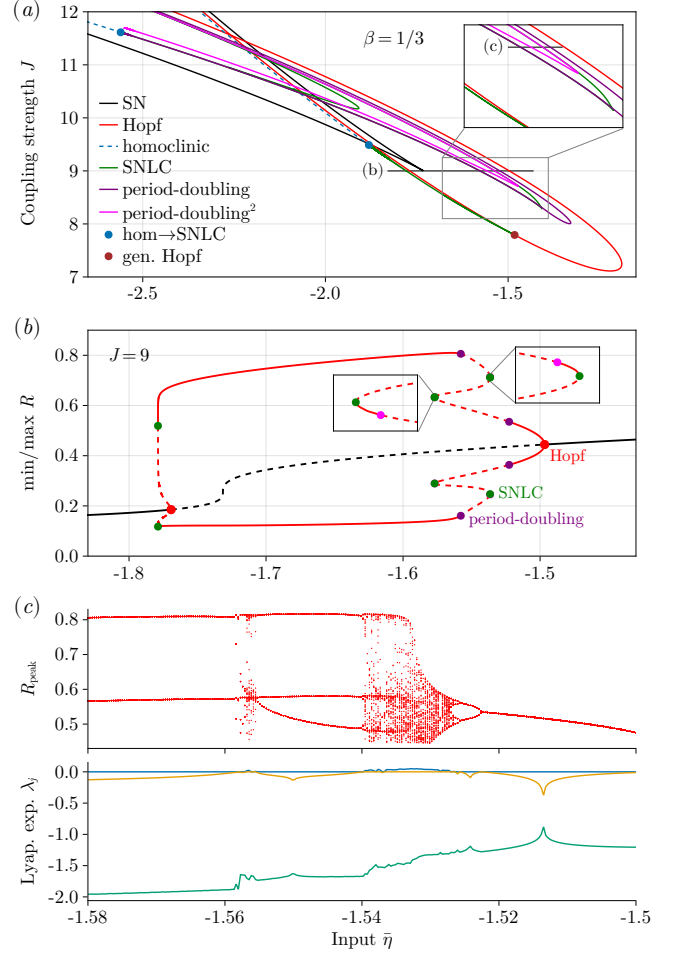


FIG. S2: Collective oscillations and macroscopic chaos exist already for small QSFA. (a) Phase diagram for $\beta = 1/3$ (zoom into the loop of Fig. S1a) with more complicated bifurcation lines. (b) Bifurcation diagram R^* vs. $\bar{\eta}$ for $\beta = 1/3, J = 9.0$. (c) Route to chaos and first three Lyapunov exponents along the black line in the inset in (a).

nant oscillatory collective behavior in Fig. S1 first becomes larger and eventually completely unties as collective oscillations expand into the $\bar{\eta} > 0$ -plane (Fig. 3b-d). For intermediate QSFA strengths, collective oscillations outside of the tiny loop require a substantial amount of recurrent excitation ($J \gg 30$ for $\beta = 1/2$, see Fig. 3c). The larger β , the stronger the activity-dependent self-inhibition and moderate recurrent excitation suffices to generate oscillatory collective dynamics. At the same time, the intricate bifurcation structure inside the loop dissolves and more complex oscillatory behavior can safely be confined within a region bounded by a period-doubling bifurcation (purple curve in Fig. 4). Here, the macroscopic chaos emerges more clearly through a period-doubling cascade and for quite a large range of parameter values (Fig. 5). In sum, stronger QSFA facilitates collective oscillations and macroscopic chaos, but these generic features can also be obtained for small QSFA as seen in Appendix B 2.